OPEN ACCESS
IOP Publishing | Songshan Lake Materials Laboratory Materials Futures
Mater. Futures 1 (2022) 015101 (9pp) https://doi.org/10.1088/2752-5724/ac3257

Si nanoparticles seeded in carbon-coated Sn nanowires as an anode for high-energy and high-rate lithium-ion batteries

Liubin Ben[1,2,3,4], **Jin Zhou**[1,2,3,4], **Hongxiang Ji**[1,2,3], **Hailong Yu**[1,2,3], **Wenwu Zhao**[1,2,3] **and Xuejie Huang**[1,2,3,*]

[1] Songshan Lake Materials Laboratory, Dongguan 523808, Guangdong Province, People's Republic of China
[2] Beijing National Laboratory for Condensed Matter Physics, Institute of Physics, Chinese Academy of Sciences, Beijing 100190, People's Republic of China
[3] Center of Materials Science and Optoelectronics Engineering, University of Chinese Academy of Sciences, Beijing 100049, People's Republic of China

E-mail: xjhuang@iphy.ac.cn

Received 15 September 2021, revised 4 October 2021
Accepted for publication 22 October 2021
Published 15 December 2021

Abstract

High-capacity and high-rate anode materials are desperately desired for applications in the next generation lithium-ion batteries. Here, we report preparation of an anode showing a structure of Si nanoparticles wrapped inside Sn nanowires. This anode inherits the advantages of both Si and Sn, endowing lithiation/delithiation of Si nanoparticles inside the conducting networks of Sn nanowires. It demonstrates a high and reversible capacity of ~1500 mAh g^{-1} over 300 cycles at 0.2 °C and a good rate capability (0.2 °C–5 °C) equivalent to Sn. The excellent cycling performance is attributed to the novel structure of the anode as well as the strong mechanical strength of the nanowires which is directly confirmed by *in-situ* lithiation and bending experiments.

Supplementary material for this article is available online

Keywords: anode, Si, Sn, nanowire, electrochemical cycling

(Some figures may appear in colour only in the online journal)

1. Introduction

Rechargeable lithium-ion batteries (LIBs) have developed significantly over the past two decades for the applications in portable electronics and electric vehicles [1–3]. For the anode of LIBs, due to the outstanding cycling performance of graphite, it was the earliest candidate and is still the most commonly candidate in today's commercial LIBs [4]. However, graphite anodes are becoming extremely problematic to meet the demands of next-generation LIBs due to its relatively low capacity of 372 mAh g^{-1} as well as poor rate capability. Recently, lithium-alloys with high capacity have attracted considerable attention for applications in next-generation LIBs [5–13]. Alloys involving Si and Sn are particularly interesting for the applications of anode materials due to their superior theoretical specific capacities of 4200 mAh g^{-1} [14, 15] and

---

[4] Co-first authors.
[*] Author to whom any correspondence should be addressed.

2752-5724/22/015101+9$33.00

Future perspectives
The combination of silicon (high lithium-ion storage capability) with tin (fast lithium-ion transport capability) widens the boundary for the anode materials of both high-capacity and high-rate for LIBs. The synthesis method is also applicable for seeding many other NPs with a high melting point to NWs with a low melting point, which shed lights on preparation of novel structured composite materials for LIBs as well as other applications.

990 mAh g^{-1} [16–19], respectively, calculated from the ultimately lithiated products. Nevertheless, the alloying of both $Li_{4.4}Si$ and $Li_{4.4}Sn$ results in drastic volume expansion of approximately 300%, leading to the fracture and pulverization of the electrode, an unstable solid electrolyte interface. Furthermore, the expansion will cause disconnection between anode components, and consequently, poor electrochemical performance [20–23].

To overcome the above problems such anode materials, many works have been undertaken, focusing on constructing Sn and Si anode materials with various morphologies to tolerate this volume change. Si nanoparticles (NPs) [24, 25], nanowires (NWs) [15], and thin films [26] have been prepared and results showed considerably enhanced electrochemical performance. Similar morphologies have also been produced for Sn anode materials [17, 27–30]. Unfortunately, Si or Sn have not yet been successfully commercialized due to their limitations. Though the theoretical capacity of Si is high, it shows a poor electrical conduction with a value of only $\sim 10^{-3}$ S cm^{-1} [31]. Previous works also showed that the lithium diffusion of Si is many orders lower than that of Sn [32]. Although carbon coating may alleviate the conduction issues of Si to some extent, it can lead to many drawbacks, such as reduced specific capacity and lower columbic efficiency [33, 34]. In contrast, both electronic [35] and ionic conductivities of Sn are high [36], but its specific capacity is only 990 mAh g^{-1}. Investigations on composite anodes have demonstrated interesting electrochemical and structural information; however, the cycling performance has only been marginally improved.

In this work, we designed an anode showing Si NPs (∼30 nm) are wrapped (seeded) inside the NWs of Sn (SiNPs-in-SnNWs), which inherits the capacity advantage of Si and the conductivity advantage of Sn. The synthesis of the anode was via a facile method similar to that reported previously [37, 38], The theoretical capacity is 1608 mAh g^{-1}, based on the starting material with a mole ratio of Si:Sn = 1:1. Electrochemical performance the anode exhibited a high and stable capacity and a good rate capability. A combination of characterization techniques directly explained the excellent capacity retention and rate capability of the anode material.

2. Methods

2.1. Materials synthesis

The anode consists of Si NPs wrapped inside Sn NWs (SiNPs-in-SnNWs) was prepared by heat-treated of mixed Si (∼30 nm) and SnO_2 (∼200 nm) powders. The mole ratio of the Si and SnO_2 mixture was 1:1. The mixture was placed in a quartz boat in the center of a tube furnace for heat-treatment at 700 °C for 2 h. A mixture gas of C_2H_2/Ar was flowing into the furnace. At high temperature, SnO_2 NPs were reduced to Sn NPs, which further changed into NWs. After the heat-treatment, a black powder was obtained. In addition, for comparison, SiNPs and SnNWs were also prepared with the similar conditions.

2.2. Materials characterization

The morphology was investigated by a scanning electron microscope (SEM, Hitachi S-4800), combined with a focused ion beam (FIB). A Bruker D8 Advance x-ray diffractometer with Cu Kα radiation ($\lambda = 1.5405$ Å) was used to collect *ex-situ* x-ray diffraction (XRD) patterns. The scan range for the XRD analysis was 10°–80° for all the samples. *In situ* XRD analysis upon galvanostatic cycling was also carried out using a self-designed *in situ* cell. After resting, the cell was galvanostatically cycled at a current rate of C/15 between 2 and 0.005 V with a constant voltage step at the lower cut-off voltage. *In situ* lithiation under scanning transmission electron microscope (STEM) was performed by constructing a NW of SiNP-in-SiNWs as the anode, and the counter electrode was a bulk of Li metal under a JEM-ARM 200F transmission electron microscope operated at 200 kV. The solid electrolyte was unavoidable surface oxidation on the Li metal. A constant voltage (−2 V) was applied through an external source meter. The lithiation process started instantaneously once the contact was established between the SiNPs-in-SnNWs and the Li electrode. The process stopped until no significant changes of the morphology of the NW were observed. *In situ* bending experiment under STEM was performed by pressing the above NW of SiNPs-in-SnNWs with the bulk of the Li metal.

2.3. Electrochemical cycling

The anode slurry was obtained by mixing the SiNPs-in-SnNWs powders with sodium alginate and carbon black (weight ratio 8:1:1). The slurry was then spread on a copper foil, followed by drying in a vacuum oven for 12 h at 110 °C. The half-cell was prepared in a 2032-type coin-cell in a Ar-filled glovebox. The counter electrode was Li metal and the separator was Celgard 2250. A 1.0 M $LiPF_6$ in a 1:1 (volume ratio) of DEC: EC was used as the electrolyte, with 2 mol% FEC as electrolyte additive. The galvanostatic cycling was performed on a LANHE CT2001A battery tester. The cut-off voltage was 0.8–0.005 V (vs. Li/Li^+). The theoretical capacity of the SiNPs-in-SnNWs is ∼1608 mAh g^{-1}, calculated from the initial Si/Sn mixture (mole ratio of 1:1). For each half-cell, the loading level was ∼10 mg cm^{-2}. For comparison with the SiNPs-in-SnNWs electrode, separate electrodes of SiNPs and SnNWs were also prepared.

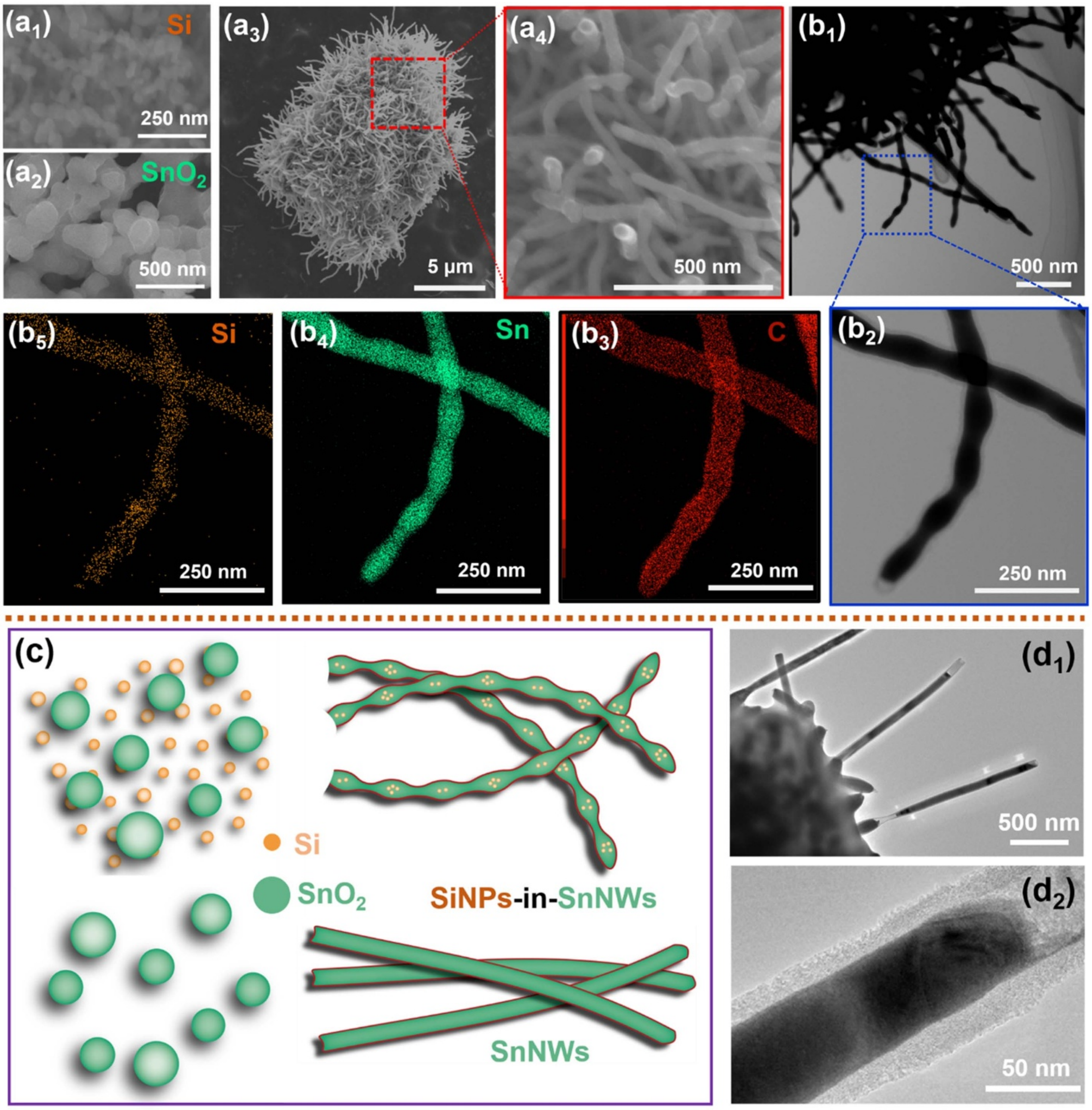

Figure 1. A typical SEM image of (a_1) Si and (a_2) SnO_2 NPs and (a_3), (a_4) SiNPs-in-SnNWs anode. (b_1), (b_2) STEM-BF images of SiNPs-in-SnNWs with the green bean shaped NWs and associated EDS mapping of (b_3) C, (b_4) Sn, and (b_5) Si. (c) Schematic showing the formation of Si NPs seeded in Sn NWs with green bean shaped NWs and Sn NWs with straight shaped NWs. (d_1) and (d_2) STEM-BF images of SnNWs with straight shaped NWs.

3. Results

3.1. Morphology, structure, and formation mechanism of SiNPs-in-SnNWs

The anode was prepared using a mixed nano-sized Si (∼30 nm in diameter, figure 1(a_1)) and nano-sized SnO_2 (∼200 nm, figure 1(a_2)) particles in flowing C_2H_2/Ar gas at 700 °C. The XRD patterns of the Si and SiO_2 starting materials are shown in figure S1 (available online at stacks.iop.org/MF/1/015101/mmedia). After the heat-treatment, large agglomerates of NWs with a length of ∼1–2 μm (∼60 nm in diameter) were obtained, and are seen in figures 1(a_3)–(a_4). Further investigation was performed by cutting the agglomerates of NWs with a FIB. A typical cross-sectional SEM image of the cut agglomerate, shown in figure S2, demonstrates a 3D structure consisting of a significant number of voids between the NWs. STEM, figures 1(b_1) and (b_2), combined with energy dispersive spectroscopy (EDS), elemental mapping of the NWs clearly shows the presence of silicon, tin, and carbon, figures 1(b_3)–(b_5).

The formation mechanism of the NWs is a vapor-solid reaction growth as described in the literature [39, 40]. Sn atoms in SnO_2 are initially reduced from the oxidation state +2 to 0 in the flowing C_2H_2/Ar atmosphere. These unstable Sn atoms may aggregate into more stable nanosized Sn clusters. At the reaction temperature 700 °C, many of the Sn nanoclusters should be in the liquid state. They could diffuse on the surface, coalesce with each other, and grow anisotropically into wires.

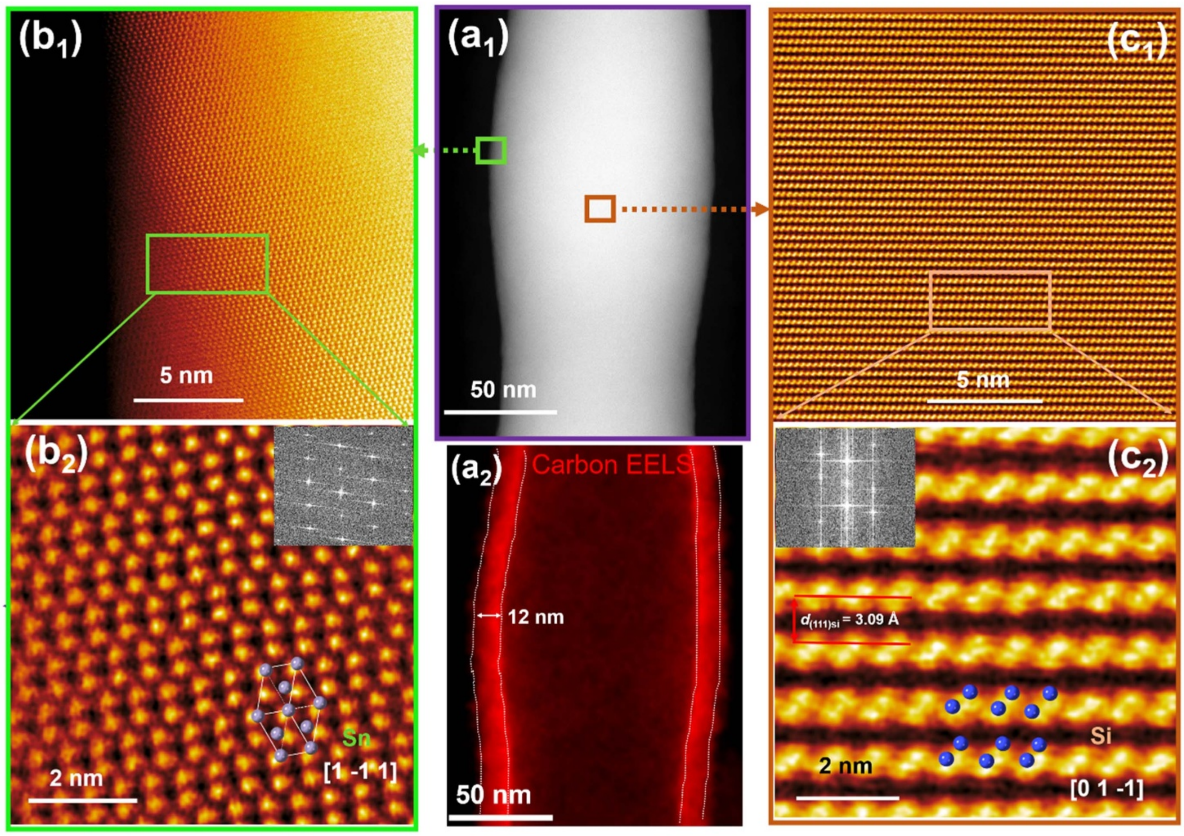

Figure 2. (a_1) A low-magnification STEM-HAADF image of a part of NW of the SiNPs-in-SnNWs anode and (a_2) corresponding EELS mapping of elemental carbon. (b_1) and (b_2) Enlarged surface regions of panel a_1. (c_1) and (c_2) Enlarged centre regions of panel a_1. FFTs corresponding to the surface ($I4_1$/amd) and center (*F*d-3m) regions are inlaid in panels b_2 and c_2, respectively. The detailed index of FFTs is shown in supporting information figure S7.

With the presence of solid-state Si NPs whose melting temperate is ∼1410 °C, liquid-state Sn nanoclusters grow on solid-state Si NPs to form 'green bean' shaped NWs. In contrast, without the presence of Si NPs, only Sn NWs are obtained with relatively straight shape. Schematic of the formation of Si NPs seeded in Sn NWs with green bean shaped NWs and Sn NWs with straight shaped NWs is shown in figure 1(c). For comparison, STEM images of the Sn NWs prepared in a manner similar to SiNPs-in-SnNWs in also shown in figures 1(d_1), (d_2) and EDS elemental mapping is shown in supporting information figure S3.

The Rietveld refinement of the XRDs of the SiNPs-in-SnNWs anode confirms that they are indeed a mixture of Sn (space group $I4_1$/amd) [41] with a small amount of Si (space group *F*d-3m) [42], figure S4. There is no evidence of the presence of SnO or SnO_2. Reflections associated with carbon are not observed, likely attributed to its limited amount or amorphous nature. The mole ratio of Si and Sn calculated from the Rietveld refinement method is generally agreed with ICP measurements (table S1) and the initial starting materials. TG analysis revealed that the amount of carbon is ∼7.0 wt%, figure S5. The amounts of carbon detected by ICP is 7.2 wt%, similar to that of TG analysis. Furthermore, the oxygen concentration in all the anode materials is minimal. XPS analysis also confirms the presence of mainly Sn and limited oxygen in the anode, figure S6.

3.2. *STEM analysis of SiNPs-in-SnNWs*

By employing a Cs-corrected STEM, the structured anode with SiNPs seeded in the SnNWs is directly revealed for the first time. A typical STEM-HAADF image of the NW is shown in figure 2(a_1). EELS mapping of carbon in the SiNPs-in-SnNWs anode clearly shows surface coverage by a ∼12 nm layer of carbon after the heat-treatment, figure 2(a_2). The presence of oxygen is minimal, according to the EELS mapping analysis. The enlarged STEM images of the surface regions of the NWs in figures 2(b_1) and (b_2), clearly demonstrate an arrangement of atoms analogous with that of Sn ($I4_1$/amd) viewed in the [1 −1 1] crystallographic direction. Fast Fourier transforms (FFTs) of the surface region (inlaid in panel b_1) and simulated reflections (figures S7(a_1)–(a_3)), further confirm the reflections of the surface region to agree with a tetragonal structure. The detailed index of FFTs is shown in figure S7. In contrast, when appropriately tilted, the central region of the NW shows a layered-like arrangement of atoms with an interlayer distance of 3.09 Å, figures 2(c_1) and (c_2), in agreement with the Si (*F*d-3m) viewed along the [0 −1 1] direction. FFTs of the center region (inlaid in panel c_1) and simulated reflections (figures S7(b_1)–(b_3)), respectively, further confirm the reflections of this region to be associated with the cubic structure. The above analysis of STEM-HAADF images and STEM-EDS mapping confirms that the SnO_2 NPs

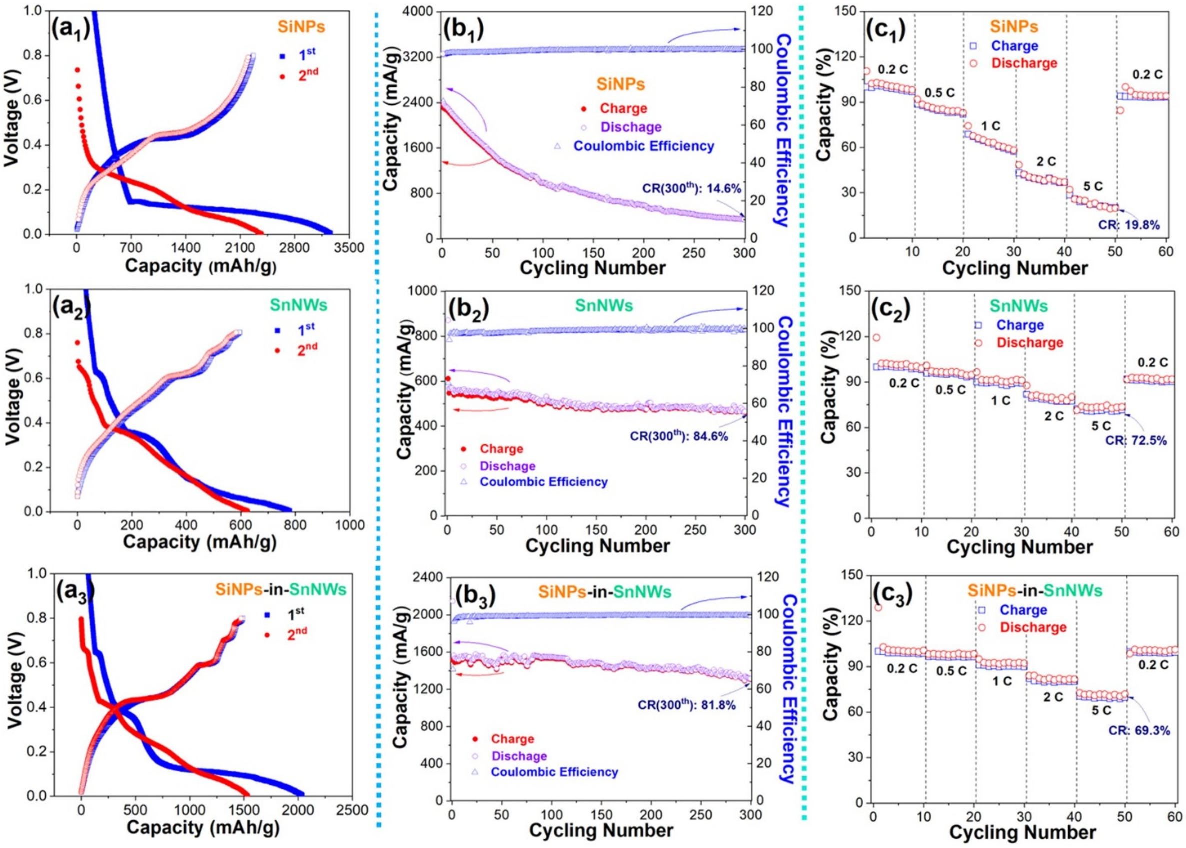

Figure 3. Electrochemical performance of SiNPs, SnNWs, and SiNPs-in-SnNWs half-cells. Charge–discharge curves (at 0.2 °C) in the 1st and 2nd cycles for (a_1)–(a_3) SiNPs, SnNWs, and SiNPs-in-SnNWs half-cells. Capacity retention and coulombic efficiency over 300 cycles (at 0.2 °C) at room temperature for (b_1)–(b_3) SiNPs, SnNWs, and SiNPs-in-SnNWs half-cells, respectively. Rate capability (0.2 °C–5 °C) for (c_1)–(c_3) SiNPs, SnNWs half-cells and SiNPs-in-SnNWs, respectively.

are converted to the SnNWs with SiNPs seeded in the latter after the heat-treatment.

3.3. *Electrochemical cycling*

The SiNPs-in-SnNWs anode naturally inherits the advantages of Si and Sn. Meanwhile, the presence of voids between the carbon-coated NWs can reduce the volume expansion during lithium insertion, guaranteeing excellent capacity retention. Figure 3 shows the cycling of the SiNPs-in-SnNWs half-cell at 0.2 °C, along with that of SiNPs and SnNWs half-cells for comparison. For SiNPs half-cell, although its initial discharge capacity is high (~3259 mAh g^{-1}), which quickly decreases with cycling (figures 3(a_1), (b_1)), and it is only ~500 mAh g^{-1} after the 300th cycle. The Sn NWs half-cell shows a stable and reversible discharge capacity of only ~600 mAh g^{-1}, though its capacity retention is 84.6% after the 300th cycle (figures 3(a_2) and (b_2)). In contrast, the SiNPs-in-SnNWs half-cell exhibits an first cycle discharge capacity of 2036 mAh g^{-1}, a charge capacity of 1488 mAh g^{-1}, and a coulombic efficiency of 73.1%, figure 3(a_3). The coulombic efficiency increases to 96.3% (2nd cycle) after the initial cycle and remains ~99.0%. The capacity retention is 81.8% after the 300th cycle, figure 3(b_3).

A major issue for an anode of high capacity, primarily of Si, is the poor electrical conductivity resulting in poor rate capability at high current densities, making them unfavorable for LIBs [6, 43]. This could be solved entirely in the SiNPs-in-SnNWs anode where SiNPs are seeded in SnNWs of fast electronic and ionic conduction. For a conventional SiNP half-cell, the capacity decreases quickly to ~19.8% from 0.2 °C to 5 °C, figure 3(c_1). In contrast, the capacity remains 69.3% for SiNPs-in-SnNWs half-cell (figure 3(c_3)), which is equivalent to that of SnNWs half-cell of 72.5% at 5 °C (figure 3(c_2)). The improved rate capability of the SiNPs-in-SnNWs anode is attributed to the increased electrical conduction and is confirmed by electrochemical impedance spectroscopy of the half-cell, as shown in figure S8.

3.4. *dQ/dV analysis*

The lithiation and delithiation of Si and Sn in the SiNPs-in-SnNWs anode can be further understood via combined d*Q*/d*V* and *in-situ* XRD investigations. The d*Q*/d*V* of the charge–discharge process (1st and 2nd) of SiNPs-in-SnNWs half-cell is shown in figure 4, along with SiNPs and SnNWs half-cells for comparison. In general, the d*Q*/d*V* (after the 1st cycle) of SiNPs-in-SnNWs half-cell (figure 4(a_3)) is a mixture that of SiNPs (figure 4(a_1)) and SnNWs (figure 4(a_2)). Reduction peaks at ~0.10 and ~0.25 V and Sn ~ 0.40, ~0.52, and ~0.64 V are associated with lithiation of Si and Sn,

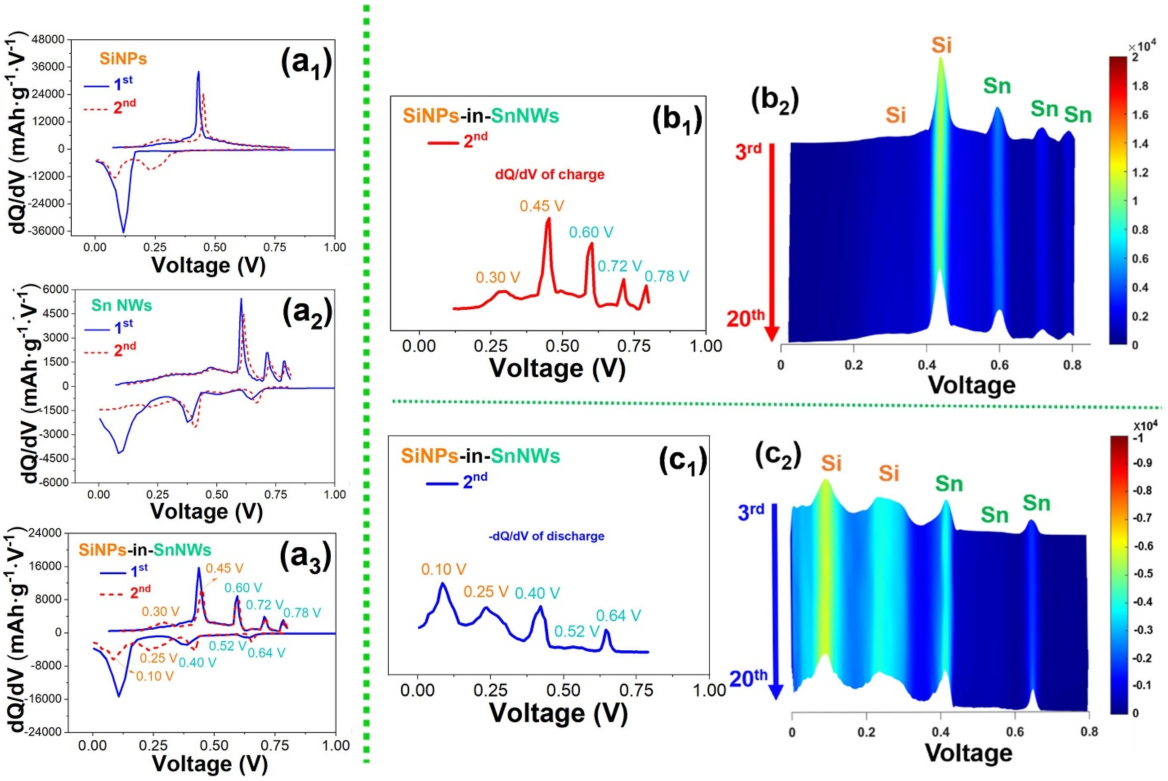

Figure 4. The first and second dQ/dV curves for (a_1) SiNPs, (a_2) SnNWs and (a_3) SiNPs-in-SnNWs. dQ/dV curves of the SiNP-in-SnNWs half-cell during (b_1) 2nd charge and (b_2) 3rd–20th charge cycles. −dQ/dV curves of the SiNP-in-SnNWs half-cell during (c_1) 2nd discharge and (c_2) 3rd–20th discharge cycles.

respectively. Oxidation peaks at ∼0.30 and ∼0.45 V and ∼0.60, ∼0.72 and ∼0.78 V are associated with associated with delithiation of Li_xSi and Li_xSn, respectively [9, 10, 44].

The dQ/dV curves as a function of voltage of the SiNP-in-SnNWs half-cell during prolonged charge and discharge cycles are separated into the dQ/dV curves during the charge cycle and −dQ/dV curves during the discharge cycle. Note the dQ/dV curves during the discharge cycle are plotted as −dQ/dV for better observation purpose. An example of the separation of the dQ/dV curves of the second charge–discharge cycle is shown in figures 4(b_1), and (c_1). The dQ/dV curves during the third to the twentieth charge cycles (figures 4(b_1) and (b_2)) and −dQ/dV curves during the second to the twentieth discharge cycles (figures 4(c_1) and (c_2)) clearly demonstrate stable peaks associated with lithiation and delithiation of Si and Sn, respectively.

3.5. In-situ *XRD analysis*

The lithiation and delithiation of Si and Sn in the SiNPs-in-SnNWs anode was investigated by *in-situ* XRD, figure 5. The C-rate during the experiment was 0.05 °C. Successive XRD scans (140 scans for the first discharge, 112 scans for the first charge) were collected (figure 5(a_1)), which were converted into an isoplot for the purpose clearer presentation (figure 5(a_2)). The detailed peak intensity associated with voltage is also shown in figures 5(b_1)–(b_4) and (c).

In general, the results show that the lithiation of the SiNPs-in-SnNWs initially follows the formation of discrete Li–Sn phases, i.e. Li_2Sn_5, β-LiSn, and $Li_{22}Sn_5$ [42, 45], followed by the formation of Li–Si phases [41, 46], which generally correlates with the dQ/dV curves. Briefly, upon discharge, a drastic decrease in intensity of the Sn peaks (e.g. 200, 101) is observed immediately upon the first discharge, figures 5(a_2) and (b_1). When the voltage is below ∼0.35 V, the Sn peaks become invisible. As the discharging proceeds, peaks (e.g. 001) associated with a Li_2Sn_5 phase start to appear, figures 5(a_2) and (b_2), and when the voltage is <0.29 V, peaks (e.g. 010) associated with a β-LiSn phase are observed, figures 5(a_2) and (b_3). On further discharging the half-cell to <0.27 V, peaks (e.g. 066) of a $Li_{22}Sn_5$ phase appear and grow in intensity, figures 5(a_2) and (b_4) [45]. During the remainder of the discharge (0.27–0.005 V), these peaks maintain their intensity, and no peaks associated with other phases are observed. The formation of Li–Si phases during discharge is generally similar to that reported previously [45]. The peak intensity associated with Si (111) remains constant until the voltage approaches ∼0.21 V, at which point Sn is lithiated to $Li_{22}Sn_5$, figures 5(a_2) and (c), which is also in agreement with previous works [41, 46].

The results suggest that the lithiation and delithiaton of Sn reaction occurs before that of Si. The formed Li–Sn phases act as a nano-size conducting network for a further Li–Si lithiation and delithiation, resulting in improved rate capabilities in the SiNPs-in-SnNWs anode, explaining the electrochemical results observed above.

The phase change behavior of the SiNPs-in-SnNWs during the first charge is generally in the reverse order of that

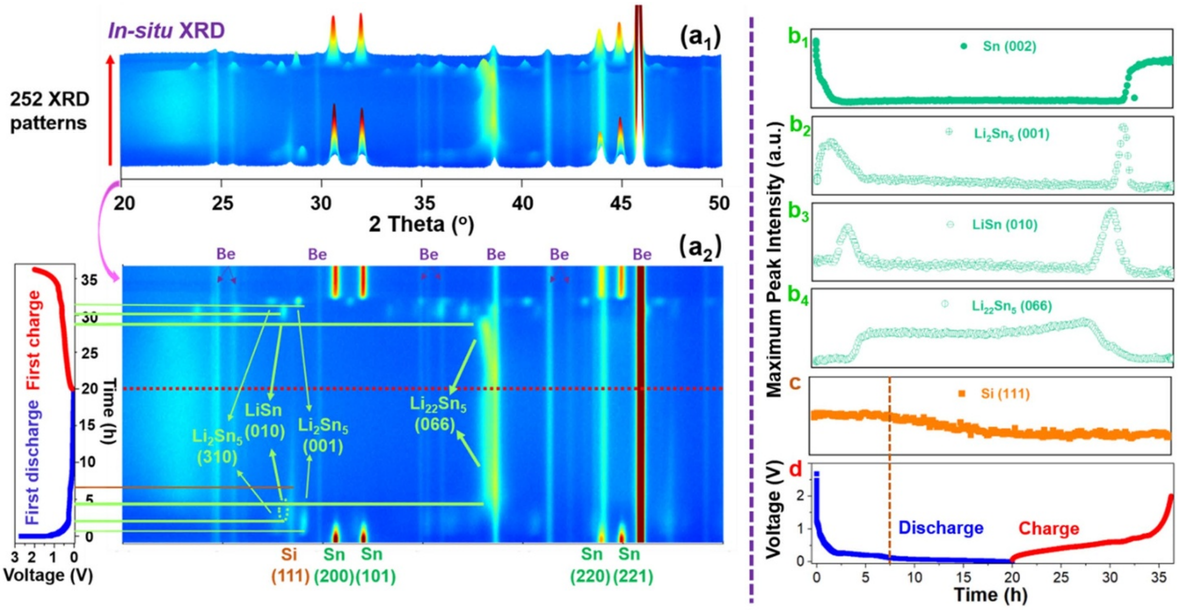

Figure 5. (a_1) *In-situ* XRD scans (140 scans for the first discharging cycle, 112 scans for the first charging cycle and 130 scans for the second discharging cycle) collected, (a_2) an isoplot converted from the collected XRD scans. Charge–discharge curves in the first-charge, first discharge and second charge cycle for the *in-situ* XRD experiment is also shown. The maximum peak intensity extracted from the *in-situ* XRD patterns for the (b_1) Sn (002), (b_2) Li_2Sn_5 (001), (b_3) LiSn (010), (b_4) $Li_{22}Sn_5$ (066) and (c) Si (111) peaks. Charge discharge curves in the first cycle are shown in (d). The dashed line across panels d indicates the start of the decrease in the Si (111) peak intensity. The unit a.u. in the panel is the abbreviation of arbitrary unit.

observed in the first discharge with slight variations. It shows that immediately upon charging, no significant change in the peaks was observed before the voltage reached >0.50 V, at which point peaks of $Li_{22}Sn_5$ (e.g. 660) shifted to a lower angle, figures 5(a_2) and (b_4). Such shifting was not observed during the first discharge. This may be associated with the phase transformation of $Li_{22}Sn$ to $Li_{17}Sn$, before transforming into LiSn. Further increasing the voltage to >0.60 V, the shifted peaks diminished, and the peaks of LiSn became detectable, figures 5(a_2) and (b_3). Upon voltage >0.62 V, peaks from both $Li_{22}Sn_5$ and LiSn were no longer detected. The formation of the Li_2Sn_5 during the first charge was first detected >0.61 V and faded away until completely it disappeared at 0.72 V, figures 5(a_2) and (b_2). Peaks from a Sn phase were first observed when the voltage was >0.68 V and grew until the end of charging, as shown in figures 5(a_2) and (b_1).

The amorphization of Si occurs irreversibly in the first discharge cycle, resulting in absence of the Si (1 1 1) peak in the following cycles [9, 44]. However, as shown in figure 4, the dQ/dV curves clearly demonstrate the stable lithiation and delithiation of SiNPs inside the SnNWs after the first charge–discharge cycle.

3.6. Mechanical stability analysis

The SiNPs-in-SnNWs anode exhibits excellent morphology without showing strong evidence of fracture or pulverization after 100th cycle at RT (0.2 °C), figures 6(a_1) and (a_2). This behavior is attributed to the unique structure of SiNPs seeded in SnNWs as explained above and the good mechanical strength of the NWs themselves [15, 47]. The latter is further confirmed via an *in-situ* lithiation and bending experiment under STEM. A sequence of STEM images of a typical NW undergoing continuous lithiation is shown in figures 6(c_1)–(c_3). The images were captured at time intervals of approximately one second and the experiment stopped until no significant changes of the morphology. The *in-situ* lithiation shows that the initial thickness of the NW is 54.8 nm in width (figure 6(c_1)), which expands immediately to 55.8 nm after lithiation (after 1 s, figure 6(c_2)). The final stable width of the NW reaches 57.6 nm (after 15 s, figure 6(c_3)), indicating an expansion of the NW of only 46.9%. The video for the *in-situ* lithiation is supplied as supporting information V1.

The NW was further stressed after lithiation by applying stress to the above lithiated NW using a Li_2O tip. A sequence of STEM images of a typical NW undergoing a continuous stress process after lithiation is shown in figures 6(d_1) and (d_2) (video supplied as supporting information V2). The bending strain of the NW was calculated according to the traditional formula $\varepsilon_{\text{bent}} = r/(r + R)\%$ [48], where R is the bending curvature, r is the radius of the NW, and $\varepsilon_{\text{bent}}$ is the largest bending strain (figure 6(d_3)). The strain in the NW increases to approximately 21.8% (figure 6(d_1)), with a strain rate of approximately 5.5 s^{-1} (after 4 s). The NW completely recovers to its original morphology without showing any fracture when the stress is removed (figure 6(d_2)), with a remarkably high strain rate of 7.3 s^{-1} (after 3 s) The observations are direct evidence responsible for the excellent cycling performance of the anode.

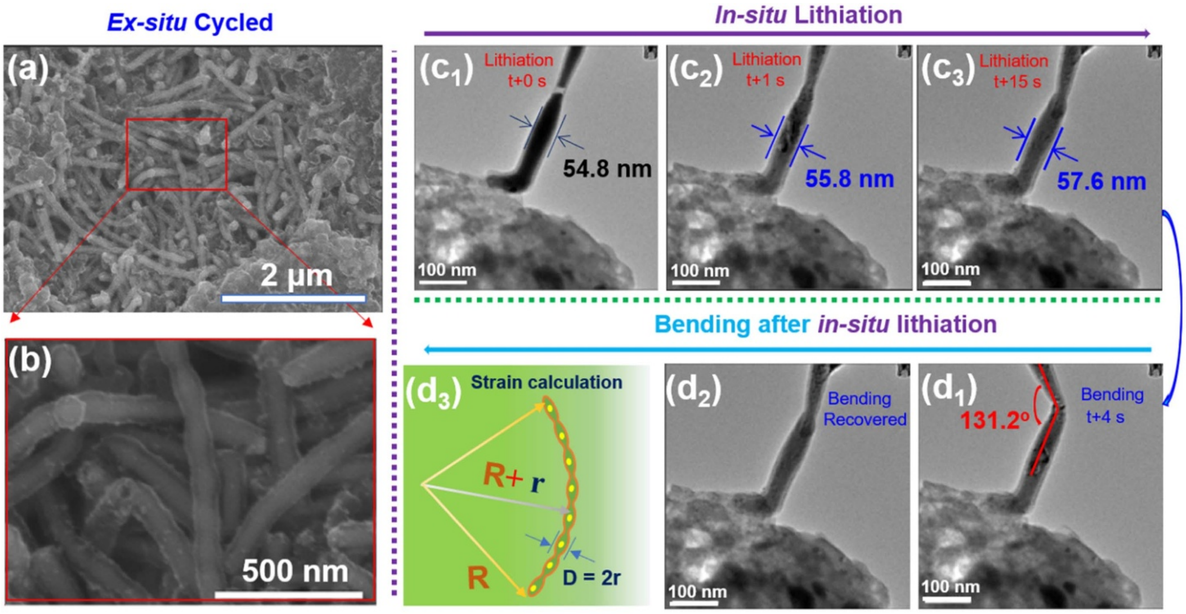

Figure 6. (a$_1$) and (a$_2$) A SEM image of the SiNPs-in-SnNWs anode after the 100th cycle. (c$_1$)–(c$_3$) a series of low-magnification STEM images of a continuous lithiation process of a single NW of SiNPs-in-SnNWs anode material. The total lithiation time is 15 s. (d$_1$) and (d$_2$) a series of low-magnification STEM images of a continuous bending and recovery process of a single NW of SiNPs-in-SnNWs anode after lithiation. The bending time is 4 s and the recovery time is 3 s. (d$_3$) schematic shows the calculation of the bending strain.

4. Conclusion

In summary, the excellent electrochemical cycling performance of the anode is attributed to the novel structure consisting of SiNPs seeded in SnNWs. This anode has the advantages of the high specific capacity of Si and the high electrical conductivity of Sn. The SnNWs provide shorter lithium-ion diffusion distances due to their narrow diameter and long continuous paths for electron transport down their length, resulting in improved rate capability. The SnNWs also endow lithiation/delithiation of SiNPs in the conducting networks of SnNWs, solving the poor conduction issue of Si during cycling. The strong mechanical strength of the NWs and the structure with a highly porous architecture allows volume variation, leading to significantly improved capacity retention after prolonged cycling.

Acknowledgments

This work was supported by the Key Research and Development Program of Guangdong Province, China (2019B121204002). Liubin Ben and Zhou Jin contributed equally to this work.

ORCID iD

Liubin Ben https://orcid.org/0000-0001-5900-678X

References

[1] Tarascon J M and Armand M 2001 Issues and challenges facing rechargeable lithium batteries *Nature* **414** 359–67
[2] Armand M and Tarascon J M 2008 Building better batteries *Nature* **451** 652–7
[3] Goodenough J B and Kim Y 2010 Challenges for rechargeable Li batteries *Chem. Mater.* **22** 587–603
[4] Aurbach D, Markovsky B, Weissman I, Levi E and Ein-Eli Y 1999 On the correlation between surface chemistry and performance of graphite negative electrodes for Li ion batteries *Electrochim. Acta* **45** 67–86
[5] Idota Y, Kubota T, Matsufuji A, Maekawa Y and Miyasaka T 1997 Tin-based amorphous oxide: a high-capacity lithium-ion-storage material *Science* **276** 1395–7
[6] Li H, Huang X, Chen L, Zhou G, Zhang Z, Yu D, Mo Y J and Pei N 2000 The crystal structural evolution of nano-Si anode caused by lithium insertion and extraction at room temperature *Solid State Ion.* **135** 181–91
[7] Chen J and Cheng F Y 2009 Combination of lightweight elements and nanostructured materials for batteries *Acc. Chem. Res.* **42** 713–23
[8] Li H, Wang Z X, Chen L Q and Huang X J 2009 Research on advanced materials for Li-ion batteries *Adv. Mater.* **21** 4593–607
[9] Park C M, Kim J H, Kim H and Sohn H J 2010 Li-alloy based anode materials for Li secondary batteries *Chem. Soc. Rev.* **39** 3115–41
[10] Xu Y H, Zhu Y J, Liu Y H and Wang C S 2013 Electrochemical performance of porous carbon/tin composite anodes for sodium-ion and lithium-ion batteries *Adv. Energy Mater.* **3** 128–33
[11] Obrovac M N and Chevrier V L 2014 Alloy negative electrodes for Li-ion batteries *Chem. Rev.* **114** 11444–502
[12] Su X, Wu Q L, Li J C, Xiao X C, Lott A, Lu W Q, Sheldon B W and Wu J 2014 Silicon-based nanomaterials for lithium-ion batteries: a review *Adv. Energy Mater.* **4** 1300882–905
[13] Aravindan V, Lee Y S and Madhavi S 2015 Research progress on negative electrodes for practical Li-ion batteries: beyond carbonaceous anodes *Adv. Energy Mater.* **5** 1402225–68

[14] Obrovac M N and Christensen L 2004 Structural changes in silicon anodes during lithium insertion/extraction *Electrochem. Solid-State Lett.* **7** A93–A6

[15] Chan C K, Peng H, Liu G, Mcllwrath K, Zhang X F, Huggins R A and Cui Y 2008 High-performance lithium battery anodes using silicon nanowires *Nat. Nanotechnol.* **3** 31–35

[16] Todd A D W, Ferguson P P, Fleischauer M D and Dahn J R 2010 Tin-based materials as negative electrodes for Li-ion batteries: combinatorial approaches and mechanical methods *Int. J. Energy Res.* **34** 535–55

[17] Chen J S and Lou X W 2013 SnO_2-based nanomaterials: synthesis and application in lithium-ion batteries *Small* **9** 1877–93

[18] Li Z, Ding J and Mitlin D 2015 Tin and tin compounds for sodium ion battery anodes: phase transformations and performance *Acc. Chem. Res.* **48** 1657–65

[19] Liu Y C, Zhang N, Jiao L F and Chen J 2015 Tin nanodots encapsulated in porous nitrogen-doped carbon nanofibers as a free-standing anode for advanced sodium-ion batteries *Adv. Mater.* **27** 6702

[20] Liu X H, Zhong L, Huang S, Mao S X, Zhu T and Huang J Y 2012 Size-dependent fracture of silicon nanoparticles during lithiation *ACS Nano* **6** 1522–31

[21] Jo H, Kim J, Nguyen D T, Kang K K, Jeon D M, Yang A R and Song S-W 2016 Stabilizing the solid electrolyte interphase layer and cycling performance of silicon-graphite battery anode by using a binary additive of fluorinated carbonates *J. Phys. Chem.* C **120** 22466–75

[22] Mao O, Dunlap R A and Dahn J R 1999 Mechanically alloyed Sn-Fe(-C) powders as anode materials for Li-ion batteries-I. The Sn2Fe-C system *J. Electrochem. Soc.* **146** 405–13

[23] Li H, Shi L H, Lu W, Huang X J and Chen L Q 2001 Studies on capacity loss and capacity fading of nanosized snsb alloy anode for Li-ion batteries *J. Electrochem. Soc.* **148** A915–A22

[24] McDowell M T, Lee S W, Nix W D and Cui Y 2013 25th anniversary article: understanding the lithiation of silicon and other alloying anodes for lithium-ion batteries *Adv. Mater.* **25** 4966–84

[25] Zhang X H, Kong D B, Li X L and Zhi L J 2019 Dimensionally designed carbon-silicon hybrids for lithium storage *Adv. Funct. Mater.* **29** 24

[26] Liu J, Yang Y, Lyu P, Nachtigall P and Xu Y 2018 Few-layer silicene nanosheets with superior lithium-storage properties *Adv. Mater.* **30** 1800838

[27] Zhou X S, Yu L and Lou X W 2016 Nanowire-templated formation of SnO_2/carbon nanotubes with enhanced lithium storage properties *Nanoscale* **8** 8384–9

[28] Li Q Q *et al* 2019 Real-time TEM study of nanopore evolution in battery materials and their suppression for enhanced cycling performance *Nano Lett.* **19** 3074–82

[29] Xu H, Li S, Zhang C, Chen X L, Liu W J, Zheng Y H, Xie Y, Huang Y and Li J 2019 Roll-to-roll prelithiation of Sn foil anode suppresses gassing and enables stable full-cell cycling of lithium ion batteries *Energy Environ. Sci.* **12** 2991–3000

[30] Wu H B, Chen J S, Lou X W and Hng H H 2011 Synthesis of SnO_2 hierarchical structures assembled from nanosheets and their lithium storage properties *J. Phys. Chem.* C **115** 24605–10

[31] Pollak E, Salitra G, Baranchugov V and Aurbach D 2007 *In situ* conductivity, impedance spectroscopy, and *ex situ* Raman spectra of amorphous silicon during the insertion/extraction of lithium *J. Phys. Chem.* C **111** 11437–44

[32] Ding N, Xu J, Yao Y X, Wegner G, Fang X, Chen C H and Lieberwirth I 2009 Determination of the diffusion coefficient of lithium ions in nano-Si *Solid State Ion.* **180** 222–5

[33] Xue L, Xu G, Li Y, Li S, Fu K, Shi Q and Zhang X 2013 Carbon-coated Si nanoparticles dispersed in carbon nanotube networks as anode material for lithium-ion batteries *ACS Appl. Mater. Interfaces* **5** 21

[34] Zhou M, Cai T, Pu F, Chen H, Wang Z, Zhang H and Guan S 2013 Graphene/carbon-coated Si nanoparticle hybrids as high-performance anode materials for Li-ion batteries *ACS Appl. Mater. Interfaces* **5** 3449

[35] Tamura N, Ohshita R, Fujimoto M, Fujitani S, Kamino M and Yonezu I 2002 Study on the anode behavior of Sn and Sn-Cu alloy thin-film electrodes *J. Power Sources* **107** 48–55

[36] Shi J J, Wang Z G and Fu Y Q 2016 Density functional theory study of diffusion of lithium in Li-Sn alloys *J. Mater. Sci.* **51** 3271–6

[37] Heitsch A T, Akhavan V A and Korgel B A 2011 Rapid SFLS synthesis of Si nanowires using trisilane with *in situ* alkyl-amine passivation *Chem. Mater.* **23** 2697–9

[38] Jin Z, Ben L, Yu H, Zhao W and Huang X 2020 A facile method to synthesize 3D structured Sn anode material with excellent electrochemical performance for lithium-ion batteries *Prog. Nat. Sci.* **30** 456–60

[39] Hu J T, Odom T W and Lieber C M 1999 Chemistry and physics in one dimension: synthesis and properties of nanowires and nanotubes *Acc. Chem. Res.* **32** 435–45

[40] Wang H Y, Huang H Q, Chen L, Wang C G, Yan B, Yu Y T, Yang Y and Yang G 2014 Preparation of Si/Sn-based nanoparticles composited with carbon fibers and improved electrochemical performance as anode materials *ACS Sustain. Chem. Eng.* **2** 2310–7

[41] Wang F, Wu L, Key B, Yang X-Q, Grey C P, Zhu Y and Graetz J 2013 Electrochemical reaction of lithium with nanostructured silicon anodes: a study by *in-situ* synchrotron x-ray diffraction and electron energy-loss spectroscopy *Adv. Energy Mater.* **3** 1324–31

[42] Im H S, Cho Y J, Lim Y R, Jung C S, Jang D M, Park J, Shojaei F and Kang H S 2013 Phase evolution of tin nanocrystals in lithium ion batteries *ACS Nano* **7** 11103–11

[43] Zhou G W, Zhang Z, Bai Z G, Feng S Q and Yu D P 1998 Controlled Li doping of Si nanowires by electrochemical insertion method *Appl. Phys. Lett.* **73** 677

[44] Jin Y, Tan Y, Hu X, Zhu B, Zheng Q, Zhang Z, Zhu G, Yu Q, Jin Z and Zhu J 2017 Scalable production of the silicon-tin Yin-Yang hybrid structure with graphene coating for high performance lithium-ion battery anodes *ACS Appl. Mater. Interfaces* **9** 15388–93

[45] Rhodes K J, Meisner R, Kirkham M, Dudney N and Daniel C 2012 *In situ* XRD of thin film tin electrodes for lithium ion batteries *J. Electrochem. Soc.* **159** A294–A9

[46] Yang X-Q, McBreen J, Yoon W-S, Yoshio M, Wang H, Fukuda K and Umeno T 2002 Structural studies of the new carbon-coated silicon anode materials using synchrotron-based *in situ* XRD *Electrochem. Commun.* **4** 893–7

[47] Luo B, Wang B, Liang M H, Ning J, Li X L and Zhi L J 2012 Reduced graphene oxide-mediated growth of uniform tin-core/carbon-sheath coaxial nanocables with enhanced lithium ion storage properties *Adv. Mater.* **24** 1405–9

[48] Zheng K, Han X D, Wang L H, Zhang Y F, Yue Y H, Qin Y, Zhang X and Zhang Z 2009 Atomic mechanisms governing the elastic limit and the incipient plasticity of bending Si nanowires *Nano Lett.* **9** 2471–6